

MTDC Grids: A Metaheuristic Solution for Nonlinear Control

Muhammad Zain Yousaf ^{1,*}, Ali Raza ^{2,*}, Ghulam Abbas ³, Nasim Ullah ⁴, Ahmad Aziz Al-Ahmadi ⁴, Abdul Rehman Yasin ³ and Mohsin Jamil ⁵

¹ School of Electrical Engineering, Guangxi University, Nanning 530600, China

² Department of Electrical Engineering, University of Engineering and Technology, Lahore 54000, Pakistan

³ Department of Electrical Engineering, University of Lahore, Lahore 54000, Pakistan; ghulam.abbas@ee.uol.edu.pk (G.A.); metary@gmail.com (A.R.Y.)

⁴ Department of Electrical Engineering, College of Engineering, Taif University, Taif 21944, Saudi Arabia; nasimullah@tu.edu.sa (N.U.); aziz@tu.edu.sa (A.A.A.-A.)

⁵ Faculty of Engineering and Applied Science, Memorial University of Newfoundland, St. John's, NL A1B 3X5, Canada; engrdrmohsin@gmail.com

* Correspondence: mzainy1@gmail.com (M.Z.Y.); a.raza@uet.edu.pk (A.R.)

Abstract: This scientific paper aims to increase the voltage source converter (VSC) control efficiency in a multi-terminal high voltage direct current (MTDC) network during dynamic operations. In the proposed study, the Mayfly algorithm (MA) is used to modify the control parameters of VSC stations. Traditional strategies that modify VSC control settings using approximate linear models fail to produce optimal results because VSCs are nonlinear characteristics of the MTDC system. Particle swarm optimization (PSO) may produce optimal outcomes, but it is prone to becoming stuck in a local optimum. To modify the proportional-integral (P.I.) control parameters of the VSC station, the Mayfly algorithm, a modified form of PSO, is used. The suggested algorithm's objective function simultaneously optimizes both the outer and inner control layers. A four-terminal MTDC test system is developed in PSCAD/EMTDC to assess the benefits of the proposed algorithm. For VSCs, a comparison of classical, PSO, and proposed MA-based tuned parameters is carried out. The integral of time multiplied by absolute error (ITAE) criterion is used to compare the performance of classical, PSO, and a proposed algorithm for VSC controller parameters/gains. With an ITAE value of 6.8521×10^{-6} , the MA-based proposed algorithm computes the optimal values and outperforms its predecessor to adjust the VSCs controller gains. For (i) wind farm power variation, (ii) AC grid load demand variation, and (iii) ultimate permanent VSC disconnection, steady-state and dynamic performances are evaluated. According to the results, the proposed algorithm based MTDC system performs well during transients.

Keywords: voltage source converter (VSC); mayfly algorithm (MA); proportional-integral (P.I.) controller; multi-objective optimization; outer control layers (OCL); inner control layers (ICL)



Citation: Yousaf, M.Z.; Raza, A.; Abbas, G.; Ullah, N.; Al-Ahmadi, A.A.; Yasin, A.R.; Jamil, M. MTDC Grids: A Metaheuristic Solution for Nonlinear Control. *Energies* **2022**, *15*, 4263. <https://doi.org/10.3390/en15124263>

Academic Editor: Pawel Rozga

Received: 12 May 2022

Accepted: 7 June 2022

Published: 9 June 2022

Publisher's Note: MDPI stays neutral with regard to jurisdictional claims in published maps and institutional affiliations.



Copyright: © 2022 by the authors. Licensee MDPI, Basel, Switzerland. This article is an open access article distributed under the terms and conditions of the Creative Commons Attribution (CC BY) license (<https://creativecommons.org/licenses/by/4.0/>).

1. Introduction

Recent research reveals that multi-terminal high voltage direct current systems have emerged as a favorable solution to fulfill future network demands. Besides their significant benefits, MTDC also appears with several promising applications [1–3]. These include incorporating the proposed European super grid [4], thus integrating the off-shore wind energy into the mainland AC network [5] and enhancing the probability of the interconnection of Mediterranean solar power and North Sea wind farms with Scandinavian hydro-power plants. The MTDC system prevents capacitance currents in comparison with large AC cable transmission.

The MTDC grid can offer a flexible and robust controlled framework in the immediate future [6]. This could force the power electronics and power system corporations to formulate control techniques that enhance system security, efficiency, and reliability [7]. With the recent progress in the voltage source converter (VSC)-MTDC topology, the viability

of connecting multiple converter stations of High Voltage DC systems is achievable with reasonable control [8]. The VSC-HVDC station emerges as an appropriate MTDC grid structure to connect massive amounts of renewable energy sources, such as photovoltaics or wind-power farms [9–13].

The vector current control (VCC) method is applied to control the VSC-HVDC station. It contains two control loops: an outer control layer (OCL) and inner current control (ICC) layer [14]. Based on the associated AC grid's demands, the outer layer attains its target by regulating the reactive or active power, AC or DC voltage control, to VSCs. At the same time, ICC controls the q- and d-axis currents via a decoupled control. Both layers have a common significant element: an integral and proportional controller. The outer control layer regulates the power-sharing within the DC grid via voltage droop control and DC-link voltage in a precise range [7]. After analyzing the interrelating control layers of the MTDC network, the VSC-terminal was revealed as a complex multi-output and multi-input control system [15]; this complex architecture has various variables that demand robust and simple control [16]. Therefore, the associated P.I. parameters should be optimally adjusted and tuned, enhancing the transient and steady-state performance. However, tuning the P.I. controllers' gains for the non-linear system is challenging [17]. Classical tuning algorithms encounter complications in determining the optimized P.I. parameters [18]. Traditional algorithms tune the P.I. parameters using approximate linear models, while the VSCs are non-linear and do not deliver good results [19,20].

Various computational methods have been formulated to treat the non-linearities in the DC grids [21]. However, using these models, mis-convergence under dynamic behavior is still a significant issue. A genetic algorithm (GA) proposed computational intelligence technology to enhance the system response by tuning the controller's P.I. parameters [22,23]. Hence, a heuristic approach is better at treating the system's non-linearities. However, GA has to conduct three operations in each iteration: crossover, mutation, and selection [24]. Thus, GA shows slow convergence towards the solution, and its performance is restricted. Therefore, a particle swarm optimization (PSO), a meta-heuristic approach, was proposed to meet the aforementioned shortcomings [25–27]. In Reference [28], PSO has been implemented for the MTDC grid, showing a better performance to ensure robustness against MTDC grid operating uncertainties. However, the research by Ref. [28] reveals that PSO requires modifications to escape from a local optimum, particularly for large dimension problems.

Therefore, a new optimization technique called the MA has been developed in recent years, which has presented better convergence performance [29]. Tsafarakis and Zervoudakis proposed this algorithm, and it is the latest technique used to resolve the non-linear optimization problem [30]. MA is a hybrid approach containing the benefits of evolutionary and swarms' intelligent algorithms, such as GA [22], PSO [26], and firefly algorithms (FA). PSO requires modification to escape from a local optimum for large dimension problems [29,31]. Inspired by the flight behavior and mayflies' mating procedure, the proposed technique offers a practical yet straightforward solution and swarm intelligence [30]. The necessary amendments are performed in MA to improve the algorithm performance across large- and small-scale dimensions. Hence, it was found suitable for a complex framework.

The VSC controller has a complex framework, and tuning controller parameters require a robust yet straightforward solution [32,33]. With this in mind, the proposed research proposes and examines the multi-objective MA technique to optimize the VSC control framework [34,35]. However, compared to the existing literature, the multi-objective MA technique has not been applied to optimize multiple control settings simultaneously in terms of an ITEA, which helps to enhance the VSC performance within an MTDC grid.

Since a meshed MTDC system is the way forward in the integrated energy system, the proposed algorithm can also help to improve the control framework for remote yet massive renewable energy resources, such as off-shore grids (i.e., wind farms), with better convergence performance. A four-terminal, VSC-based MTDC test system is designed

in PSCAD/EMTDC, with two off-shore grids to conduct the dynamic simulations and evaluate the proposed architecture performance. In comparison to Refs. [25,26,36], the proposed MA technique also uses the MTDC system in-depth, but apart from a conventional solution, we also compare it with state of the unconventional art techniques. Furthermore, the design process is automated, requiring relatively little input from the designer, reducing the reliance on the designer's experience.

Under the circumstances above, the main contribution of this article is:

- The optimized P.I. controller parameters are achieved using multi-objective MA, employed in the outer and inner control layers;
- The proposed architecture addresses three control problems simultaneously: optimization, steady-state stability, and controller robustness under dynamic operations;
- Apart from numeric comparisons in terms of ITEA, MA-based optimized parameters were compared with classical-P.I. and PSO-P.I., and tested for dynamic and steady-state stability performances under the following conditions:
 - (1) Wind power variation;
 - (2) AC grid load demand variation;
 - (3) Ultimate permanent VSC disconnection.
- The proposed control architecture and a robust DC fault protection scheme can pave the path to an MTDC system based on VSCs in the future.

The rest of the paper is laid out as follows: the employed test grid's structure and mathematical modeling are presented in Sections 2 and 3. The in-depth controller evaluation is offered in Section 4, and an optimization theory is presented in Section 5. Section 6 deals with the implementation and execution. Section 7 is allocated for multi-objective optimization, followed by Section 8 with the results and simulations. Finally, Section 9 contains the conclusion.

2. Test System under Study

A four-terminal, VSC-based MTDC test grid is presented in Figure 1. Transmission lines are linked through positive and negative DC-link voltage. The DC inductor (100 mH) is connected at each end of the transmission line to exhibit a practical DC scheme. Each transmission line is 100 km long, and the DC test grid rating is presented in Table 1.

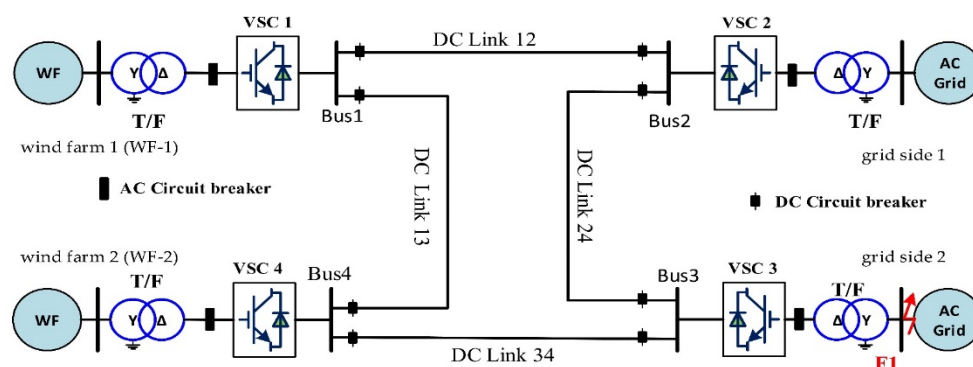
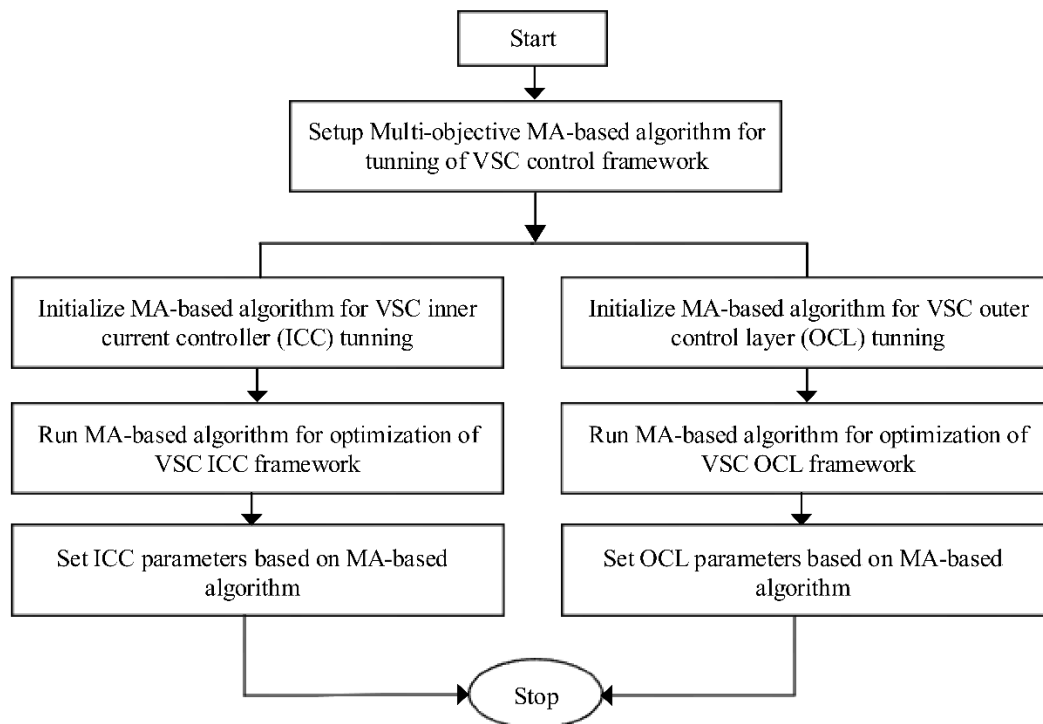


Figure 1. A four-terminal, VSC-based MTDC test grid.

Since the test system under study has a VSC-based control framework, the general implementation of the proposed algorithm for the VSC station is shown in Figure 2. The proposed algorithm aims to improve the transient and steady-state response with the help of the P.I. controller's parameter regulation. Meanwhile, a simple steady-space state model of the MTDC grid helps to describe the system's dynamic response. This can help in choosing the optimal limits and the correct parameters. For state-space analysis, simplified circuit modeling is required. The circuit modeling explained in the following sub-section helps in the state-space analysis for the proposed test system.

Table 1. Parameters of VSC-based MTDC Test Grid.

Parameters	Impedance	Nominal Voltage (kV)	Values
AC Network	0.002 + j0.01 p.u	220	1000 MW
Wind Farm	0.001 + j0.015 p.u	33	1000 MW
DC Link	L = 0.50×10^{-3} H/km R = 0.10×10^{-3} Ω /km C = 2.31×10^{-7} F/km	± 250	100 km DC link b/w all VSC Terminals
DC capacitor	Two series capacitors of 1400 μ F	± 250	

**Figure 2.** Optimization of the VSC-based control framework using the proposed algorithm.

Equivalent Circuit Model

Nodes and branches are connected to obtain an equivalent model. A four-terminal MTDC grid with two off-shore wind farms and two on-shore grids is presented in Figure 3.

The variable constraints shown in Figure 3 are:

- R_1 and R_3 represents branch resistance on-grid transmission lines.
- L_1 , L_2 , and L_3 represents branch inductances on-grid transmission lines.
- I_{L1} , I_{L2} , I_{L3} , I_{C1} , I_{C2} , $I_{C_{m+p+1}}$ and $I_{C_{m+p+2}}$ are currents flowing through different inductors and capacitors.
- C_1 , C_2 , C_{m+n+1} and C_{m+n+2} represents the equivalent capacitances of the capacitors, which are connected in parallel to the grid.
- E_1 , E_2 , E_{m+n+1} and E_{m+n+2} represents the voltages across the capacitors, which are parallel to the current sources.
- P_1 , P_2 , P_{m+n+1} and P_{m+n+2} represents the power supplied by the different converters which are connected to the respective grids.
- I_1 , I_2 , I_{m+n+1} and I_{m+n+2} represents currents from current sources within the HVDC grid.

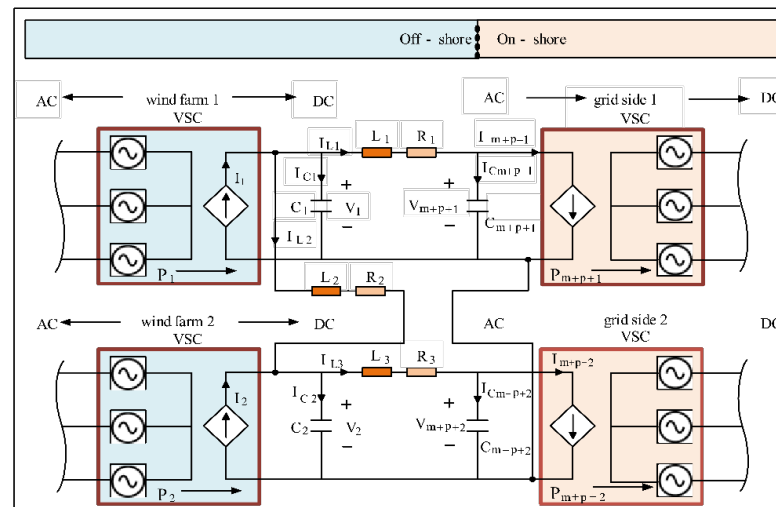


Figure 3. Four terminal VSC-based MTDC grid.

3. State-Space Representation of Four Terminal MTDC Test Systems

The dynamic performance of the MTDC grid can be described using a set of first-order differential equations. These differential equations are acknowledged as the representation of state-space and are represented in Equations (1)–(3) [11,36].

The state-space model representing the dynamic is:

$$\frac{dx_1}{dt} = Ax + B_w w + B_u u, \tag{1}$$

where x denotes state vector, $\frac{dx_1}{dt}$ represents derivative of the state vector at state point x_1 , u indicates vector of a controlled input, w represents a vector of a non-controlled input. B_u represents controlled input values in a matrix, B_w represents non-controlled input in a matrix. A represents a state of matrix, B_u represents controlled input values in a matrix, B_w represents non-controlled input in a matrix. The non-controlled output equation is:

$$z = C_z x, \tag{2}$$

where z represents a non-controlled output vector. C_z represents controlled output values in a matrix. The controlled output equation is:

$$y = C_y y, \tag{3}$$

where y represents controlled output vector and C_y represents controlled output vector in a matrix. The equivalent circuit presented in Figure 3 is for the test model illustrated in Figure 1. Thus, applying a first-order differential equation to the four-terminal MTDC system results in Equations (4)–(14) [11,36].

$$\frac{dV_1}{dt} = \frac{1}{C_1} I_{C1}, \tag{4}$$

$$\frac{dV_2}{dt} = \frac{1}{C_2} I_{C2}, \tag{5}$$

$$\frac{dV_3}{dt} = \frac{1}{C_3} I_{C3}, \tag{6}$$

$$\frac{dV_4}{dt} = \frac{1}{C_4} I_{C4}. \tag{7}$$

V_1 and V_2 represent the voltages that are input to the controller. V_3 and V_4 represent the reference voltages for V_1 and V_2 , which are to be maintained. Equations (4)–(7) represent

the derivative for these voltages. I_{C_1} is the current at capacitor C_1 . I_{C_2} is the current at capacitor C_2 . I_{C_3} is the current at capacitor C_3 .

$$\frac{dI_{L_1}}{dt} = \frac{1}{L_1}(-R_1 I_{L_1} + V_1 - V_3), \quad (8)$$

$$\frac{dI_{L_2}}{dt} = \frac{1}{L_2}(-R_2 I_{L_2} + V_1 - V_2), \quad (9)$$

$$\frac{dI_{L_3}}{dt} = \frac{1}{L_3}(-R_3 I_{L_3} + V_2 - V_4), \quad (10)$$

$$I_{C_1} = I_1 - I_{L_1} - I_{L_2}, \quad (11)$$

$$I_{C_2} = I_2 - I_{L_3} + I_{L_2}, \quad (12)$$

$$I_{C_3} = -I_3 + I_{L_1}, \quad (13)$$

$$I_{C_4} = -I_4 + I_{L_3}. \quad (14)$$

For further variables information, please refer to the text under Figure 3. Equation (15) shows enough variables to define the system's state, including four capacitors and three inductors.

$$x = [V_{C_1} V_{C_2} V_{C_3} V_{C_4} I_{L_1} I_{L_2} I_{L_3}]^T. \quad (15)$$

The input and output of the state-space model are defined in the following matrices.

$$w = [I_1 I_2]^T, u = [I_3 I_4]^T, z = [V_1 V_2]^T, y = [V_3 V_4]^T. \quad (16)$$

Since wind farms inject all the available active power to the grid sides, a rush of current is expected, so the droop control at the mainland VSC station helps to control and stabilize the DC voltage. In Equation (16), w is a vector of currents and u is the control input containing vector currents of grid sides 1 and 2, respectively. The matrices for state-space representation are expressed in Equations (17)–(21).

$$A = \begin{bmatrix} 0 & 0 & 0 & 0 & -1/C_1 & -1/C_1 & 0 \\ 0 & 0 & 0 & 0 & 0 & 1/C_2 & -1/C_2 \\ 0 & 0 & 0 & 0 & 1/C_3 & 0 & 0 \\ 0 & 0 & 0 & 0 & 0 & 0 & 1/C_4 \\ 1/L_1 & 0 & -1/L_1 & 0 & -R_1/L_1 & 0 & 0 \\ 1/L_2 & -1/L_2 & 0 & 0 & 0 & -R_2/L_2 & 0 \\ 0 & 1/L_3 & 0 & -1/L_3 & 0 & 0 & -R_3/L_3 \end{bmatrix}, \quad (17)$$

$$B_w = \begin{bmatrix} 1/C_1 & 0 \\ 0 & 1/C_2 \\ 0 & 0 \\ 0 & 0 \\ 0 & 0 \\ 0 & 0 \\ 0 & 0 \end{bmatrix}, \quad (18)$$

$$B_u = \begin{bmatrix} 0 & 0 \\ 0 & 0 \\ -1/C_3 & 0 \\ 0 & -1/C_4 \\ 0 & 0 \\ 0 & 0 \\ 0 & 0 \end{bmatrix}, \quad (19)$$

$$C_z = \begin{bmatrix} 1 & 0 & 0 & 0 & 0 & 0 & 0 \\ 0 & 1 & 0 & 0 & 0 & 0 & 0 \end{bmatrix}, \tag{20}$$

$$C_y = \begin{bmatrix} 0 & 0 & 1 & 0 & 0 & 0 & 0 \\ 0 & 0 & 0 & 1 & 0 & 0 & 0 \end{bmatrix}. \tag{21}$$

4. Control Structure Based on State-Space Analysis

This section describes the methodology used to optimize the VSC station’s control parameters using state-space analysis. The analysis in the previous section helps to choose the proper control parametric values, which can improve the system’s dynamic response. The subsequent section studied the VSC control structure and gave the optimized parametric values, using state-space analysis to confirm the results.

4.1. Control Structure of VSC Based HVDC Grid

The control diagram shown in Figure 4 represent the controller for the off-shore wind farms (wind farm 1 and wind farm 2). A controller uses a P.I. controller to fix the voltages at 50 Hz. Then, the P.I. controller minimizes the error, i.e., the difference between actual and reference RMS voltages at the terminals of wind farms, represented in Equation (22).

$$Error = V_{WF} - V_{WF}^*. \tag{22}$$

V_{WF} is the actual RMS voltage, and V_{WF}^* is the reference RMS voltage.

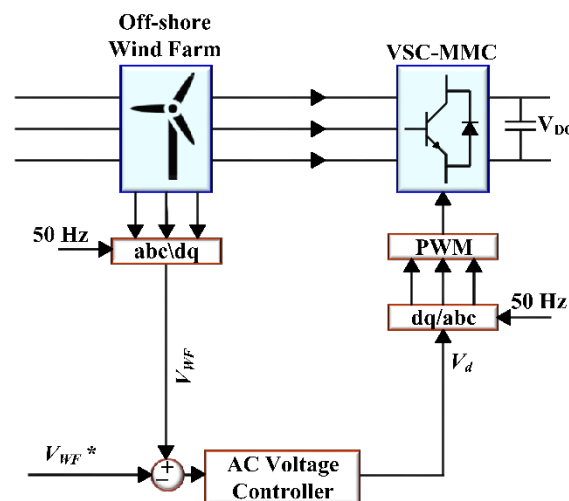


Figure 4. AC voltage controller schematic for wind farms.

The control diagram illustrated in Figure 5 presents the improved proportional droop control, which allows for the coordination of DC voltage between grid side 1 and grid side 2. $V_{g,ref}$ and P_{ref} are the DC reference voltage and active power per unit. ‘K’ shows the slope of droop characteristics, and the DC voltage at the grid side converter, with zero power, is represented by V_g per unit.

The control scheme in Figure 6 shows the control structure of the VSC-based multi-terminal HVDC system. The differential quadrature (d-q) method regulates the active or DC voltage or AC voltage, or reactive power. The d-components are in charge of DC voltage or active power control, whereas the q-components are responsible for AC voltage or reactive power regulation. Meanwhile, the parametric values of the three-phase line, such as current and voltage, convert into two dimensions, rotating the d-q referenced frame for simplicity by applying the Clark-transformation equation. Further, three-phase line parametric values are synchronized via a phase-locked loop (PLL) for abc to d-q transformation. During transformation, the outer controller generates referenced currents for the inner controller, whereas the inner current controller defines the VSC’s reference voltage for the d-q frame.

In doing so, the compensating term L_{wid} is used to decouple the d and q-axis components. These two-axis components are then fed into the d-q to abc transformation platform to perform inverse park transformation. Finally, the resulting PWM is provided to MMC at the grid side.

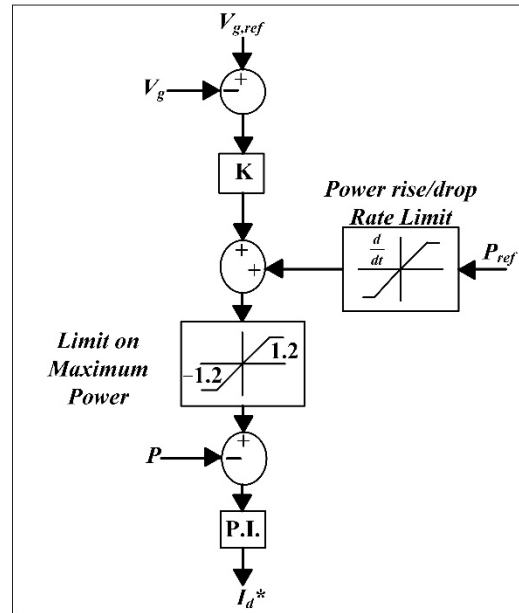


Figure 5. Improved proportional droop control.

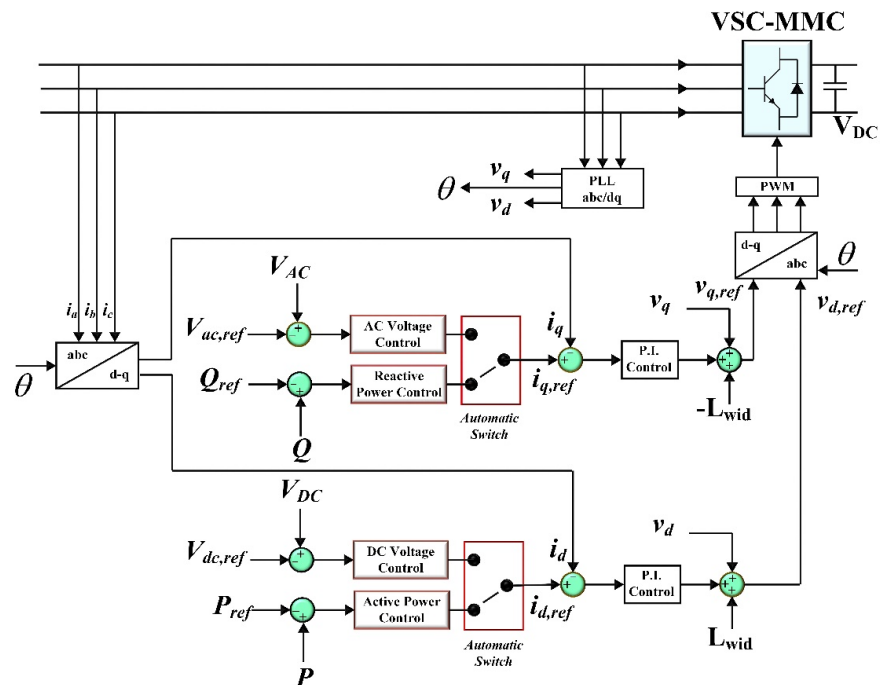


Figure 6. The control structure of the VSC-based MTDC system.

4.1.1. Outer Control Layer

Considering the inclusive dq frame, the outer controller controls the AC and DC voltage, reactive and active powers at the point of common coupling (PCC). The q-channel

controls the AC voltage or reactive power, whereas the d-channel controls the DC voltage or active power, as presented in Figure 6 and expressed as:

$$P = v_d i_d + v_q i_q, \tag{23}$$

$$Q = v_q i_d - v_d i_q, \tag{24}$$

where i_d represent the d-axis current and i_q represent the q-axis current.

The AC grid phasor voltage is synchronized with PLL, the d-axis of current vector control. Therefore, $v_q = 0$. Note that the d-axis component of the common bus voltage is denoted by v_d , while the q-axis component of the common bus voltage is represented by v_q .

$$P = v_d i_d, \tag{25}$$

$$Q = -v_d i_q. \tag{26}$$

The d–q axis currents regulate the reactive and active power using Equations (25) and (26). The AC voltage controller injects the proper amount of reactive power to control the AC voltage magnitude at the PCC, such that it resembles the given reference voltage. Likewise, the q-axis current regulates the AC voltage. The DC-link voltage is maintained at a predetermined reference value by exchanging an appropriate active power with the AC system. Thus, the d-channel current regulates the DC-link Voltage.

4.1.2. Inner Current Control

After receiving reference currents values, the inner current controller is accountable for processing these values and maintaining the reference voltage at the VSC output side. The relationship between the voltage at the VSC side (v_g) and the voltage at PCC (e_c) are presented as:

$$e_c - v_g = R \times i_c + L \times \frac{di_c}{dt}. \tag{27}$$

L and R represent the inductance and resistance between the VSC station and the PCC, while the AC current (i_c) is towards the VSC converter. By taking Park transformation:

$$e_d - v_d = R \times i_d - \omega L \times i_q + L \times \frac{di_d}{dt}, \tag{28}$$

$$e_q - v_q = R \times i_q - \omega L \times i_d + L \times \frac{di_q}{dt}, \tag{29}$$

ω is the AC system’s angular frequency at the PCC; the layout of the ICC control is presented in Figure 7. The reference signals ($v_{d,ref}$ and $v_{q,ref}$) are transformed back to the abc-frame to generate IGBTs switching.

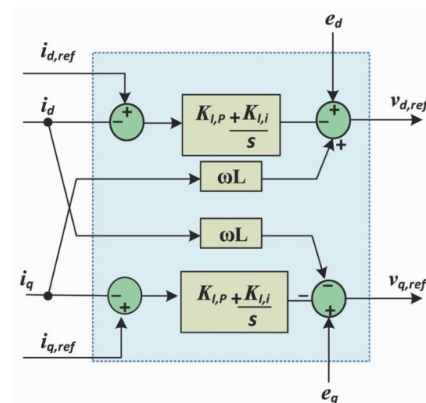


Figure 7. The control structure of an inner current controller. Adapted with permission from Ref. [26]. Copyright 2022, IEEE.

5. P.I. Controller Optimization Based on Mayfly Algorithm

The performance of a VSC-based MTDC system depends on the precise tuning of the P.I. parameters. Thus, the optimal tuning of P.I. controllers is of prime importance. This paper proposes a MA meta-heuristic technique to optimize the P.I. controller's parameters. MA offers benefits, such as a fast convergence and low susceptibility to becoming stuck at a locally optimal point. MA finds an application in engineering optimization problems, such as an optimal feature selection to reduce the training time for machine learning algorithms [29]. The Mayfly algorithm is explained below.

5.1. Mayfly Optimization Algorithm

Mayflies are insects associated with Ephemeroptera, a portion of a cluster of insects recognized as Palaeoptera. These insects primarily emerge during May in the U.K. and are identified as Mayfly. Juvenile insects devote various years developing as marine nymphs until they are ready to emerge as adult Mayflies at the water's surface. Most male adults perform a bridal dance that includes specific down and up movements, creating a pattern by gathering swarms above the water surface to fascinate the female mayflies. The mating process starts when female mayflies attract these swarms. The mating continues for only a few seconds; afterward, they lay eggs on the water surface, and the cycle lasts. A more comprehensive explanation of the above procedure is presented in the work of Guo et al. [34] and Majumdar et al. [35]. The MA mechanism is presented in a subsequent section.

5.1.1. Movement of Male Mayflies

The male Mayfly's position is modified as;

$$X_i^{T+1} = X_i^T + V_i^{T+1}, \quad (30)$$

where X_i^T represents the current position of male Mayfly, and the updated position, X_i^{T+1} is achieved by adding the velocity, V_i^{T+1} at the current position. The male Mayflies develop a good speed a few meters above the water surface. The male Mayfly's velocity is updated as:

$$V_{kj}^{T+1} = G * V_{kj}^T + b_1 * e^{-\beta r_p^2} * (pbest_{kj} - X_{kj}^T) + b_2 * e^{\beta r_g^2} * (Gbest_j - X_{kj}^T). \quad (31)$$

Here, V_{kj}^T is the k_{th} Mayfly velocity in j dimension at time T , X_{kj}^T shows the same Mayfly's position at time T . β indicates a static visibility constant used to restrict the visibility of a Mayfly to others. b_1 and b_2 are a positive fascination constant that measures the social and cognitive constituents' participation, respectively. G represents the gravitational coefficient. $pbest_k$ is the leading optimal position that a specific k_{th} Mayfly visited, and $Gbest_j$ is the j_{th} constituent of the best male Mayfly's position. Lastly, r_g is the Cartesian distance between $Gbest$ and X_k , while r_p is the Cartesian distance between $pbest_k$ and X_k . $pbest_k$ is updated as:

$$pbest_k = \begin{cases} X_k^{T+1} \\ \text{if } fit(X_k^{T+1}) < fit(pbest_k) \end{cases} \quad (32)$$

where $fit(X_k^T)$ offers the fitness value of the position that examines the solution's equality. Hence:

$$|X_k - x_k| = \sqrt{\sum_{j=1}^n (X_{kj} - x_{kj})^2}, \quad (33)$$

where x_k denotes $pbest_k$ or $Gbest$ X_{kj} indicates the j_{th} element's position of k_{th} Mayfly. Note that the best Mayflies must do a nuptial dance at a specific time, which offers a

stochastic component to the algorithm. The mathematical illustration of this nuptial dance is as follows:

$$V_{kj}^{T+1} = G * V_{kj}^T + D * r. \quad (34)$$

D is the nuptial dance coefficient, r is an arbitrary value $\in (-1, 1)$. This coefficient gradually decreases as follows: $D_{itr} = D_0 * \delta^{itr}$. itr shows the current number of iterations, D_0 is the starting value of the nuptial dance coefficient, and δ is an arbitrary value $\in (0, 1)$.

5.1.2. Movement of Female Mayflies

The male Mayflies attract the female Mayflies for mating. The female Mayfly's position is modified as:

$$Y_i^{T+1} = Y_i^T + V_i^{T+1}, \quad (35)$$

where Y_i^T indicates the present position of female Matfly at time T and the updated position, Y_i^{T+1} , is achieved by adding the velocity, V_i^{T+1} with the current position. The fascination procedure amid female and male Mayflies depends on the quality of fitness function: that is, the best male attracts the best female Mayflies. The female Mayfly's velocity is updated as:

$$V_{kj}^{T+1} = \begin{cases} G * V_{kj}^T + b_2 * e^{-\beta r_{mf}^2} * (X_{kj}^T - Y_{kj}^T) & \text{if } fit(Y_k) > fit(X_k) \\ G * V_{kj}^T + fL * r & \text{else if } fit(Y_k) \leq fit(X_k) \end{cases} \quad (36)$$

In Equation (36), Y_{kj}^T is the k_{th} female Mayfly's position in j dimension at time t , V_{kj}^T is the j_{th} element of the k_{th} female Mayfly's velocity, X_{kj}^T is the j_{th} component of k_{th} male Mayfly's position at time t . G is the previously defined gravity coefficient in (31). β and b_2 are the formerly defined visibility coefficient and fascination constant, respectively. r_{mf} is the Cartesian distance between female and male Mayflies expressed in Equation (33). r is an arbitrary value $\in (-1, 1)$, and fL is the random walk coefficient at the moment when the female is not fascinated by a male Mayfly, $fL_{itr} = fL_0 * \delta^{itr}$.

5.1.3. Mating of Mayflies

The crossover maneuver indicates the mating operation amid two Mayflies. This is achieved by choosing a male Mayfly and then a female Mayfly based on their fitness function—the best male breeds with the best female. Two offspring are generated because of this crossover, given as:

$$offspring1 = (1 - u_o * female) + u_o * male, \quad (37)$$

$$offspring2 = (1 - u_o * male) + u_o * female. \quad (38)$$

A female is the female parent Mayfly, and the male is the male parent and u_o is the arbitrary value between 1 and 0. The offspring's initial velocities are fixed as zero.

5.1.4. Mayfly's Mutation

The mutation of newly produced offspring enhances the exploration ability of the algorithm. A typically dispersed varying number is added to the variable of offspring:

$$offspring'_m = offspring_m + q. \quad (39)$$

where q is the random value of the normal distribution.

The block diagram of the MA is presented in Figure 8. The MA parameters are initialized in the first step, containing both female and male Mayflies' populations and velocities. These parameters are interrelated to the ambiguous constraint of a given problem. The particle performance is evaluated under the initially generated position by examining the performance index. In this case, the performance index is based on the integral time absolute error (ITAE) of the parametric inputs chosen for the inner and outer controller.

While optimizing, the position is updated after each iteration, and the stopping criterion is based on the given iteration index, which is 10 in this case.

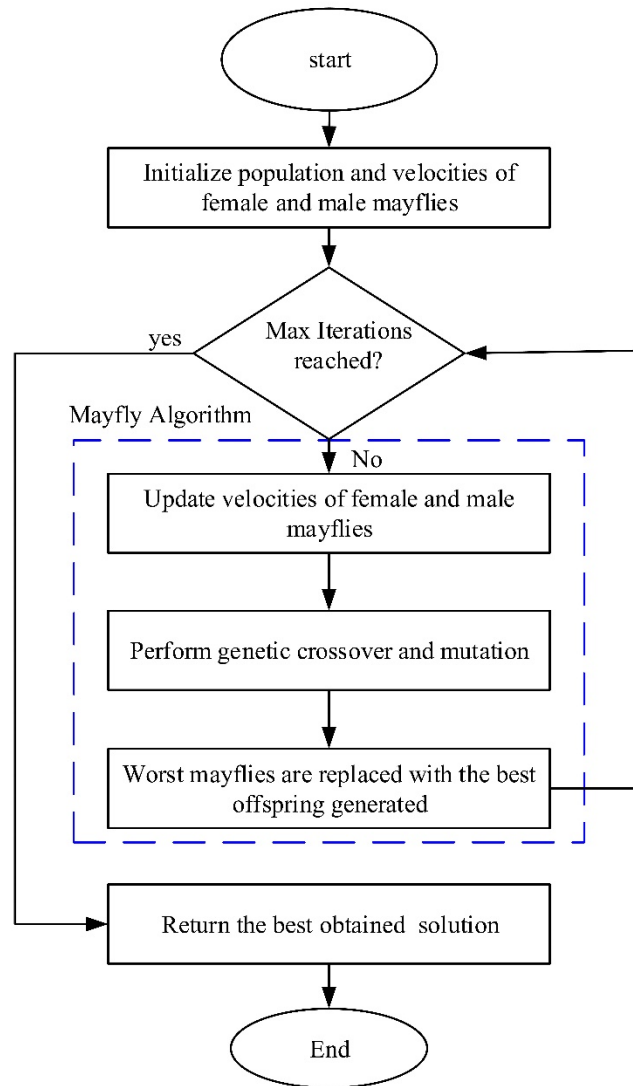


Figure 8. Flowchart of the MA.

Figure 9 reveals the block diagram of MI processing on the P.I. controllers. In conjunction, the proposed algorithm’s parameters are tabulated in Table 2.

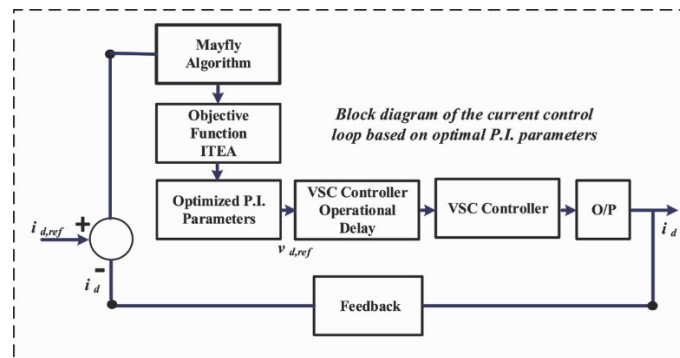


Figure 9. MA implementation of P.I. controllers.

Table 2. MA parameters.

Parameters	Values
The size of the population	20.0
Max number of iterations	10.0
The relative weightage for fitness value ($\gamma\beta$)	0.80
The positive-attraction constant (b_1 and b_2)	3.0, 3.50
Co-efficient (β)	0.10
Gravitational co-efficient (G)	0.980
Crossover random values	0.950
Acceptance rate	0.80
Range and rate of pitch adjustment	2.0 and 0.3

6. Multi-Objective Optimization of VSCs Using MA

The proposed MA algorithm can formulate a multi-objective optimization function to optimize the P.I.-controller parameters of the VSC station. The VSC essential control loops OCL and ICC are optimally tuned in a parallel application.

6.1. ICC Tuning Using MA

The core component of the VSCs controller is the inner current control layer. The MA-based multi-objective function is crucial to improving the P.I. control parameters for optimal gains. The schematic diagram of the MA scheme is shown in Figure 10. The characterized ICC objective function is formulated as:

$$Minimize : O_{ICC} = \int_0^T t \cdot |i_d - i_{d,ref}| dt. \tag{40}$$

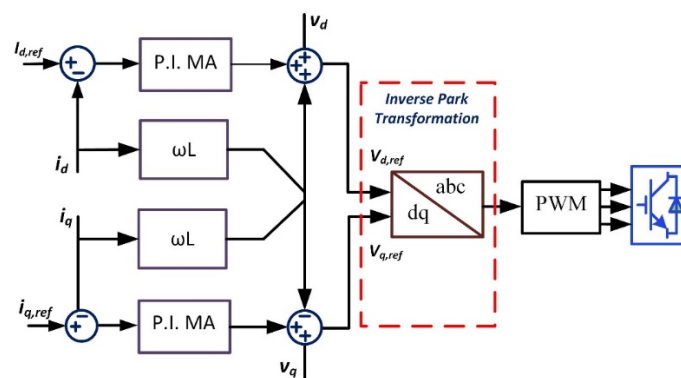


Figure 10. The control structure of ICC using MA.

6.2. OCL Tuning Using MA

The OCL control parameters are optimally tuned in parallel with the ICC control parameters in a multi-objective function. The schematic diagram of the proposed MA algorithm for the OCL is illustrated in Figure 11. The characterized objective function is formulated as follows:

$$Minimize : O_{OCL} = \int_0^T t \cdot |P - P_{ref}| dt. \tag{41}$$

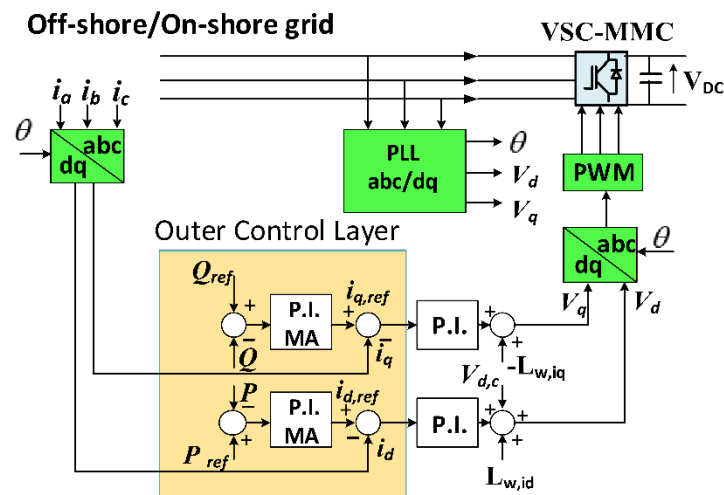


Figure 11. The control structure of OCL using MA.

7. Execution of the Multi-Objective Function

The multi-objective function (OBJ-FN) helps to minimize the simultaneous multi-objective problems. This research article aims to achieve a fast response from the MTDC system under dynamic conditions by optimizing the multi-objective function. Primarily, fundamental constrained problems are individually optimized, and afterward, the best compound solution is obtained by an active set methodology. Secondly, a weighted sum strategy is employed with the MA technique for parallel tuning of the OCL and ICC controllers' corresponding objective functions. Figure 12 shows the schematic diagram of this optimized procedure. The selection criteria for weights are user-defined, and an autonomous generated set of values [37]. In the weighted sum approach, multi-objective problems are assumed as a compound objective function that can be expressed as:

$$OBJ - FN = \sum_{m=1} w_m F_m(x) \quad m = 1, 2, \tag{42}$$

where w_m indicates non-zero weight values.

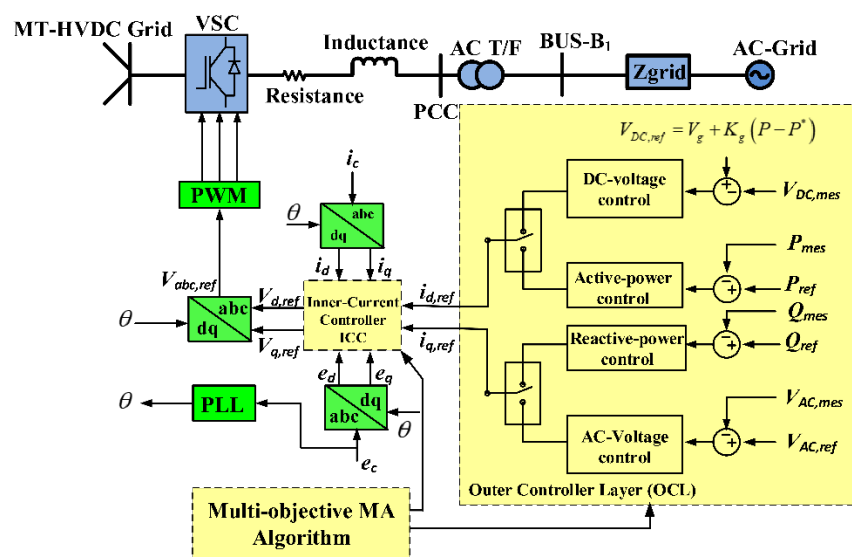


Figure 12. VSCs multi-objective tuning using MA.

The optimization aim of the multi-objective problem is obtained with the minimization of Equation (42). The purpose of this is to deliver a composition comprising two distinct objective functions: Equations (40) and (41). The compromised solution is determined by

each objective function's weight, while the weight selection describes each component's importance in Equation (43). Therefore, the objective function may be re-expressed as:

$$OBJ - FN = w_1 O_{ICC} + w_2 O_{OCL}. \quad (43)$$

The weights of w_1 and w_2 are allocated and interrelated as:

$$w_2 = 1 - w_1.$$

w_1 ranges $0 \rightarrow 1$.

Constraints for Optimization

A conventional technique is based on classical tuning [26,38]. The classical tuning approach for the inner controller is based on the following two points:

1. The closed-loop bandwidth of the inner-controller should be 1/5 times less than the switching angular frequency;
2. The inner-controller should be at least 10 times faster than the outer-controller to attain an oscillatory free response.

Therefore, the P.I. parameters of the inner controller are selected based on the technique of [26]. Meanwhile, similar steps are adopted to tune the outer controller. This is based on the fact that the inner controller should be 10 times faster than the external controller. Based on the above limitation provided for the P.I. controller parameters, the mathematical constraints for the optimization problem are expressed as follows:

At first, the k_p and k_i constraint for the inner current controller is expressed as:

$$k_p \leq \alpha_{IC} L^{p.u}, \quad (44)$$

$$k_i \leq \alpha_{IC} R^{p.u}, \quad (45)$$

where α_{IC} denotes the closed-loop bandwidth for the ICC. Meanwhile, the switching is set to 2 kHz in this work. This is illustrated as:

$$\alpha_{IC} \leq \frac{2 \times 2 \times \pi}{5} = \frac{4 \times \pi}{5} = 2.5 \text{ k rad/s}. \quad (46)$$

Thus, for the outer current controller (OCC), we have:

$$\alpha_{OC} \leq \frac{1}{10} = 0.1 \alpha_{IC}. \quad (47)$$

Further, based on the study proposed in [38], we have derived the k_p and k_i constraint for the OCC as:

$$k_p \leq \alpha_{OC} C^{p.u}, \quad (48)$$

$$k_i \leq \alpha_{OC}^2 C^{p.u}, \quad (49)$$

where α_{OC} denotes closed-loop bandwidth for the OCL. The proposed MA algorithm is executed and implemented in the subsequent section following the constraint modeling.

8. Simulation Results

The proposed MA algorithm aims to optimize the time response of the grid parameters under dynamic scenarios. First, input features were extracted multiple times in PSCAD, with each simulation having a runtime of 8 s. Second, input features were fed into the proposed algorithm to obtain optimized results to assess the validity and flexibility. Accordingly, the performance index of the proposed algorithm is shown in Figure 13. As the number of iterations increased, the algorithm evolved towards minimization, which provided optimal values for the inner and outer loops. The optimized control parameters for the inner and outer controllers are shown in Table 3. Under the notion between

Equations (44) and (49), the obtained conventional control parameters are presented in Table 4. Meanwhile, the entire process was implemented on a personal computer with specific features: an Intel-Core i5 processor with a speed of 3.2 G-Hz. Next, different scenarios were generated in the test grid to address the proposed algorithm's effectiveness against conventional and non-conventional optimal techniques to assess the performance of the optimal parameters [20].

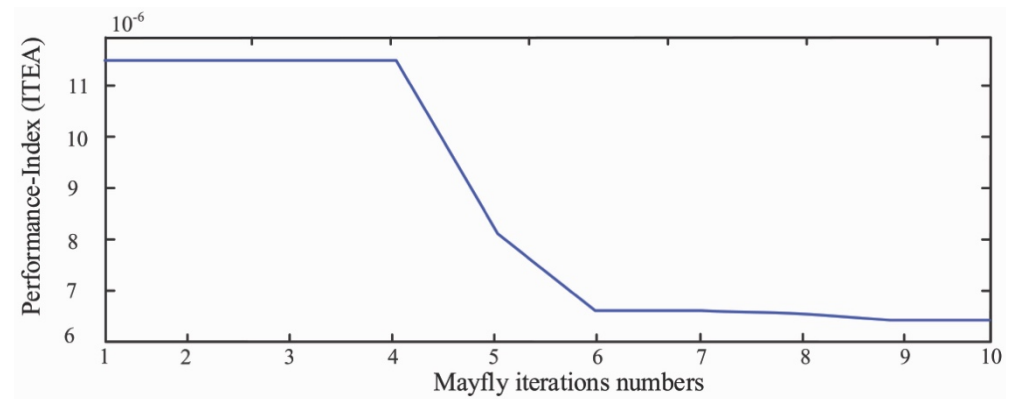


Figure 13. The performance index of Mayfly optimization for the 10 iterations.

Table 3. MA optimized parameters.

Controller	PSO Tunes P.I.	
	Kp	Ti = 1/Ki
Inner Controller	0.7686	17.7610
Outer Controller	0.7686	75.2660

Table 4. Classical parameters.

Controller	PSO Tunes P.I.	
	Kp	Ti = 1/Ki
Inner Controller	0.5193	14.9551
Outer Controller	0.1052	33.1312

8.1. Scenario I: Comparison with the Conventional Technique

In this scenario, the stability margin of the proposed and conventional control parameters is observed under the time domain. There are some constraints to follow when finding gains for the controllers [25]. Usually, the hit and trial model is utilized to find the conventional gains while considering the constraints as limits [25]. With this in mind, and following the computation in Section 7, the time response is based on MA and classical tuned control parameters tested for the ramping of wind-farm power. At first, wind farm 1 power increases from 0.4 p.u to 0.51 p.u, while wind farm 2 remains constant. This sudden change caused a rise in DC-link voltage from 1.071 p.u to 1.079 p.u. Second, the power of wind farm 2 decreases from 0.725 p.u to 0.625 p.u, respectively. From Figure 14, the Mayfly parameters clearly show significant improvements compared to the classically tuned parameters. Comparatively, the stability margin along a rising time is much better than in conventional settings.

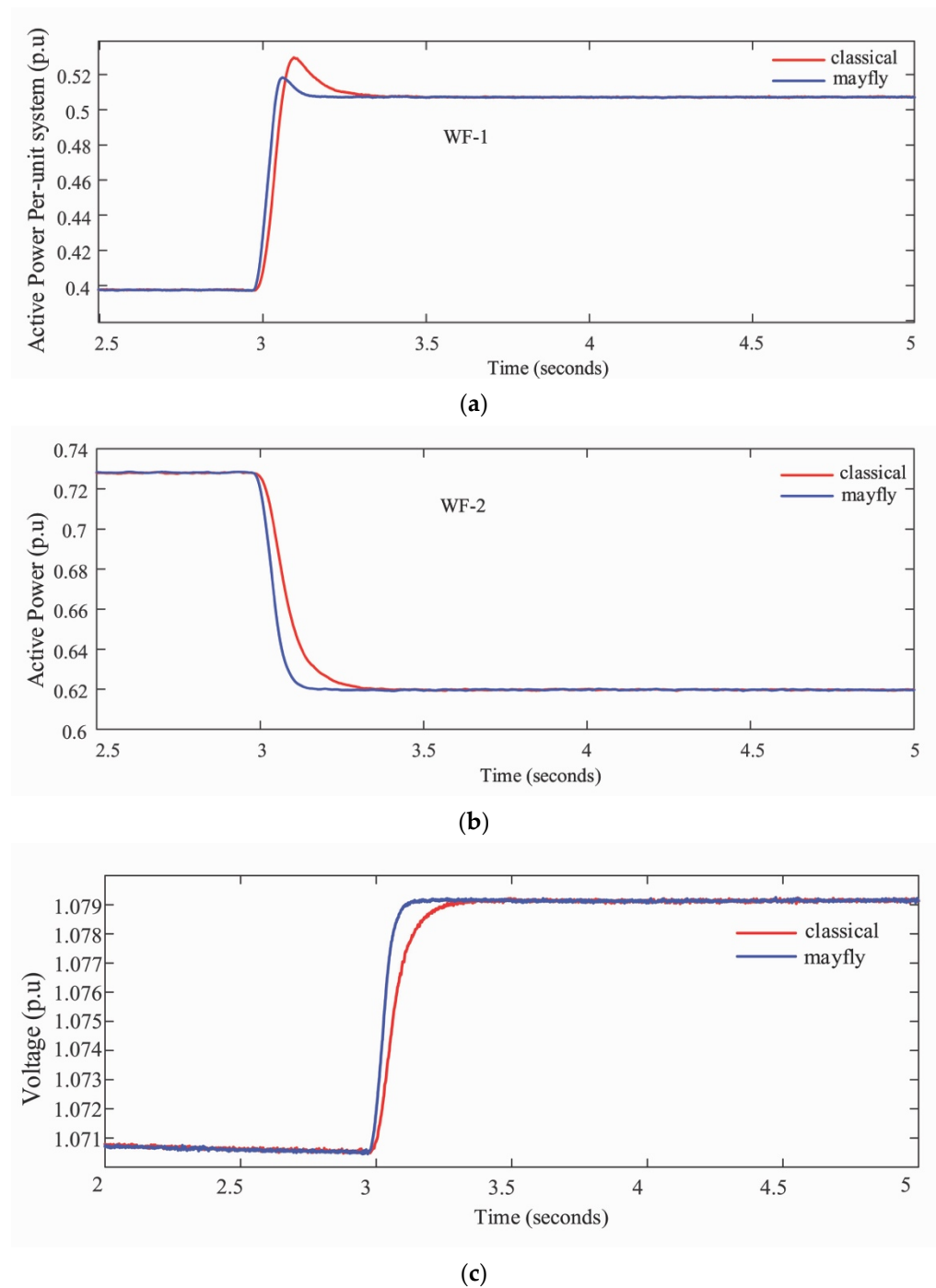


Figure 14. Change in power at wind farms (a) The change at wind farm 1. (b) The change at wind farm 2. (c) The change at DC-link voltage due to the wind farm 1.

The demand change at the grid side is studied to further test the proposed algorithm's robustness. At $t = 3.0$ s, the load demand decreased from -0.7 to -0.55 p.u. at grid side 2. This sudden change in demand also causes fluctuations in grid side 2. However, optimized grid parameters, particularly the MA-based controller, manage to settle down quickly. A graphical comparison between the Mayfly and classically tuned parameters is shown in Figure 15. The visual observation indicates that the proposed algorithm performs much better; it stabilizes the DC voltage and power profile faster than the classical technique.

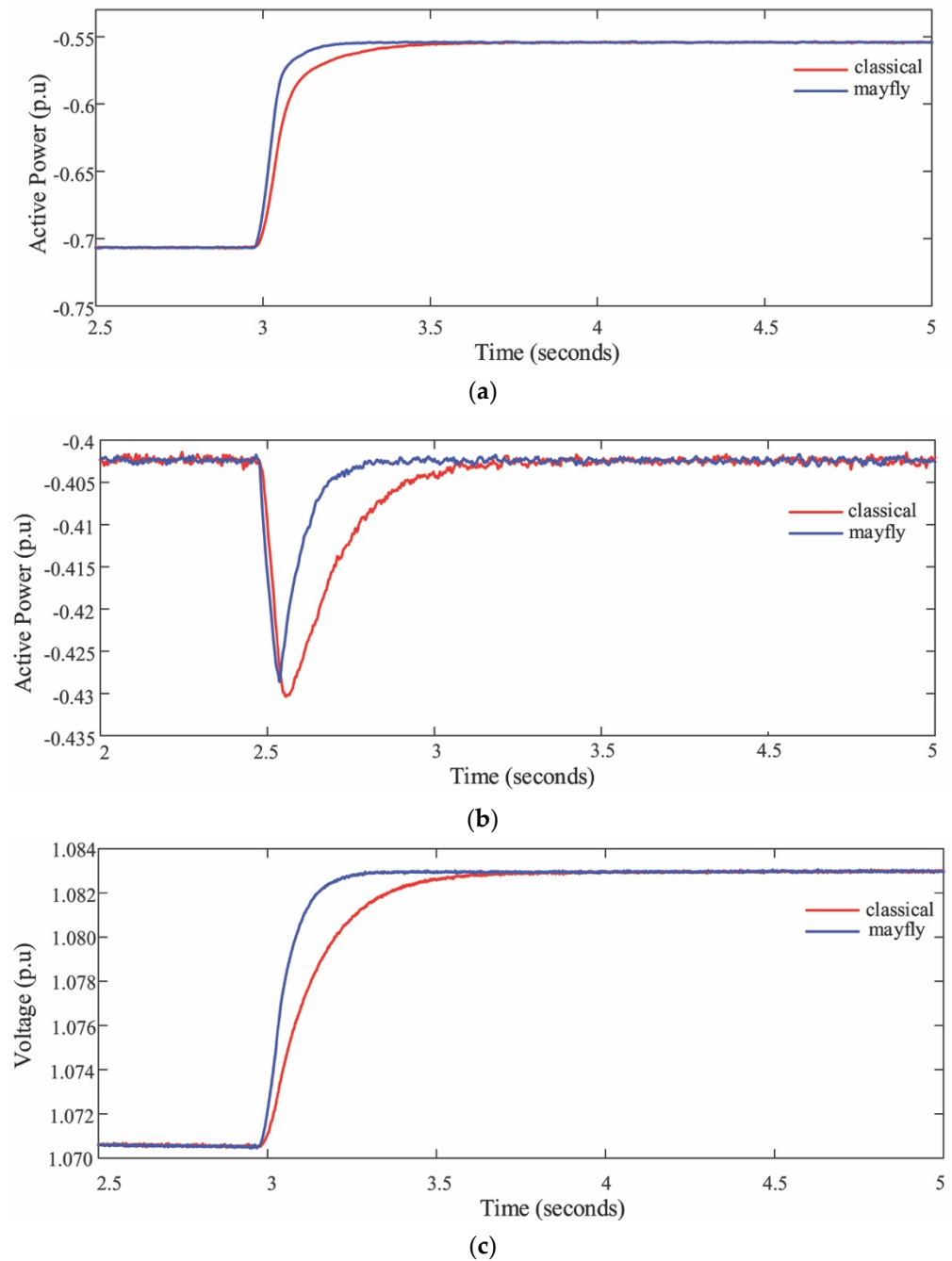


Figure 15. Power and voltage profiles at grid side 1 and grid side 2; (a) the power change at grid side 1; (b) the power change at grid side 2; (c) the change at DC-link voltage due to grid side 1.

8.2. Scenario 2: Comparison with the Unconventional Technique

The proposed algorithm was tested alongside PSO to obtain the proposed technique's desirable effects on the test grid. For enumeration, the PSO algorithm was set up under the same testing scenarios as the Mayfly algorithm, and its parameters are presented in Table 5.

Likewise, the aim was to minimize the objective function defined in Equation (42). The fitness function values using PSO optimization are shown in Figure 16, and the obtained controller parameters are given in Table 6. It is essential to highlight that, in earlier iterations, the PSO's performance index is better than a Mayfly. However, the Mayfly algorithm's convergence rate and speed for the later iterations improve the performance more than the PSO. Further, the active power profile obtained by Mayfly, PSO, and classical tuning is

shown in Figure 17. The results exhibit significant improvements and a faster rising time for Mayfly than the PSO and classical tuning.

Table 5. PSO parameters.

Parameters	Values
Max number of iterations	10.0
Values of particle	4.0
Weights (w_1 and w_2)	0.850 and 0.150
Initial population	15.0

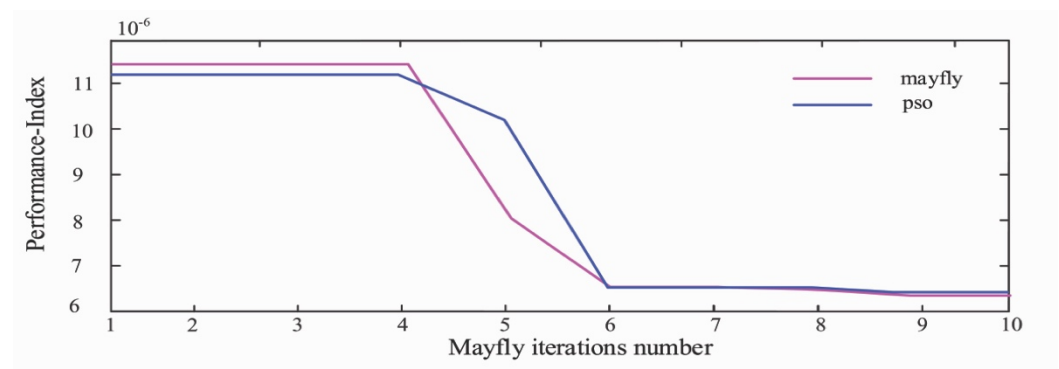
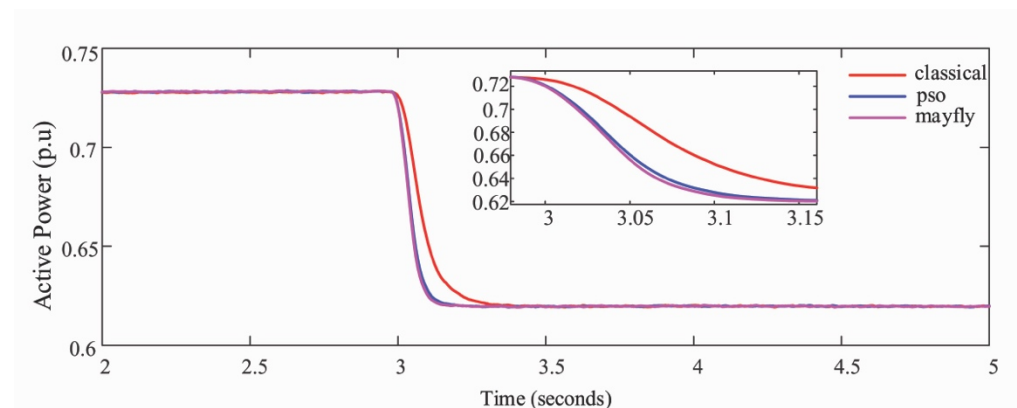
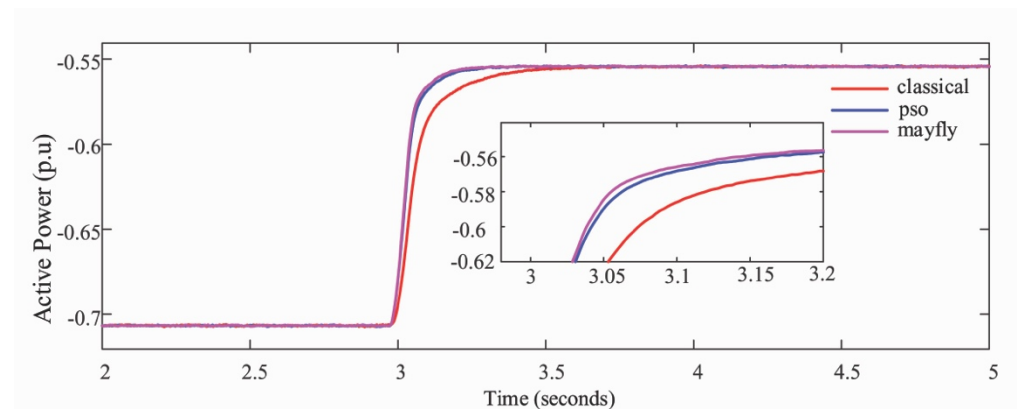


Figure 16. The performance index of PSO for the 10 iterations.



(a)



(b)

Figure 17. Change in power at wind farms: (a) power ramp at wind farm 1; (b) change in demand at grid side 2.

Table 6. PSO-based P.I. controller parameters.

Controller	PSO Tunes P.I.	
	Kp	Ti = 1/Ki
Inner Controller	0.7705	18.7910
Outer Controller	0.7705	73.2270

To present a meaningful numerical evaluation of the efficiency of Mayfly and PSO controllers, they are compared in terms of minimizing the integral time multiplied by absolute error (ITAE) measurements of (10), (11), and (13) in Table 7. Apart from PSO, recent techniques, such as Harris hawks optimization [39] and the water cycle algorithm (WCA) [40], claim to perform better in DC micro-grids but need further investigation. For example, in Ref. [40], the multi-objective approach is missing to address related problems such as load variation. Similarly, in Ref. [41], the outlined method's performance is evaluated for a linearized model of a single VSC-based HVDC system. Ultimately, a switching model of a point-to-point VSC HVDC system is built to demonstrate its use. Therefore, it also needs further investigation for the MTDC system.

Table 7. Comparison of P.I. parameters' efficiency in terms of ITEA.

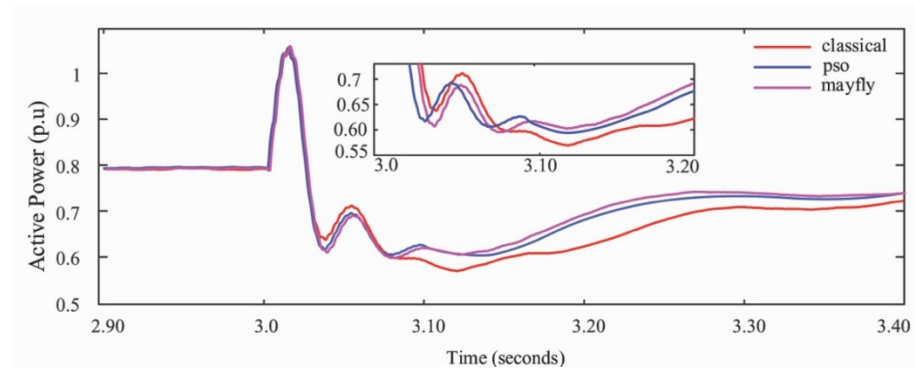
Controller Section	ITEA		
	Mayfly	Classical	PSO
Inner Controller	8.4002×10^{-6}	4.7208×10^{-4}	8.8013×10^{-6}
Outer Controller	7.6101×10^{-5}	1.7640×10^{-3}	7.7074×10^{-5}
Objective Function	6.8521×10^{-6}	-	6.9221×10^{-6}

8.3. Scenario 3: Fault Scenario

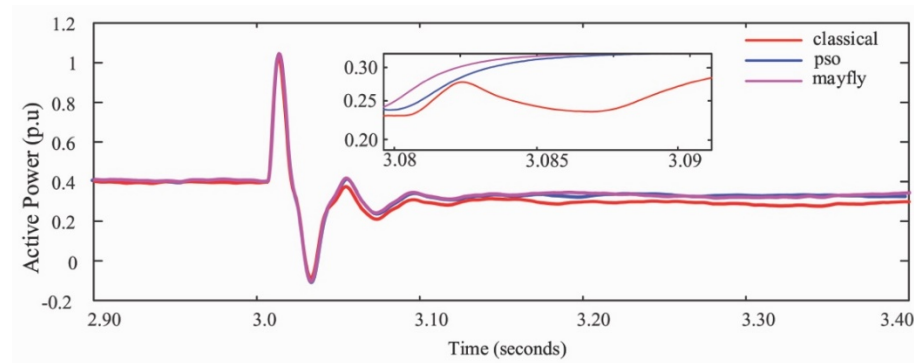
In this scenario, the stability performance of the MTDC is evaluated under a three-phase permanent fault at VSC 3 station side. For evidence, a three-phase permanent fault is introduced at time $t = 3.0$ s. The fault characteristics of the permanent fault include a fault resistance of 0.01Ω situated at the fault location F1 (According to Figure 1). Just before the fault event, the total power generated by the MMCs at the wind side was 1.2 p.u, and the grid side shared that power according to their droop control characteristics. However, when the fault occurred at grid side 2 (MMC-3), all generated power was quickly shifted towards grid side 1, and the power at grid side 2 reduced to zero. The graphical representation clearly shows that wind side grids show a slight fluctuation in their power and quickly return to their original state when the instant fault occurs.

Meanwhile, grid side 1 quickly attained the power levels required for the supply. It is indicated from Figure 18a–d that Mayfly controllers achieve better responses than their predecessors. For example, when comparing the proposed algorithm, PSO, and classical model in Figure 18a, it is clear that the MA-based model attains stability faster than the other two. Similarly, in Figure 18c, the steady-state response for the MA-based model is better, and the unwanted transient settling is also fast. Meanwhile, the DC power profile quickly achieves the desired output levels, thanks to optimum regulated settings.

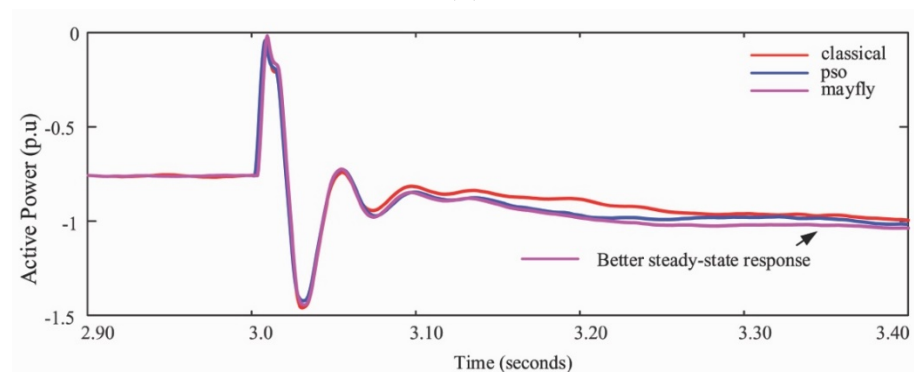
The fault current is also less severe in the Mayfly controllers at the grid side 2, as shown in Figure 19. Moreover, this phenomenon puts less strain on the HVDC grid components. In HVDC, protection is an important issue that needs consideration. Suppose this optimal technique is placed with robust fault detection and the hybrid circuit breaker. The time response would be better, but the stability margin would also improve.



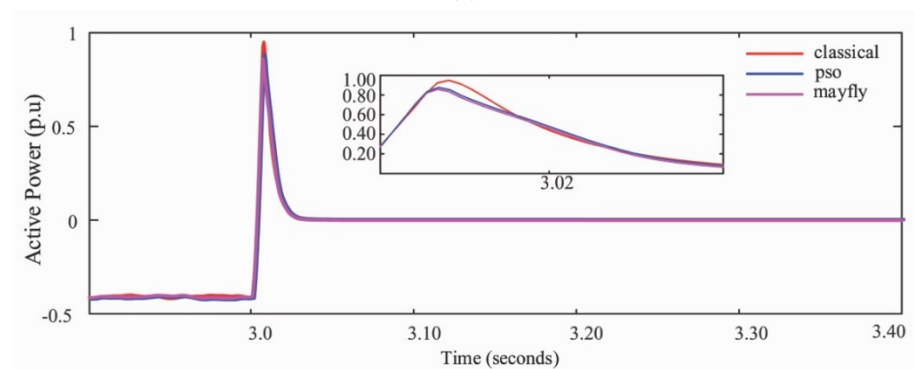
(a)



(b)



(c)



(d)

Figure 18. (a) Power fluctuation at wind farm 1, (b) power fluctuation at wind farm 2, (c) load-shifting profile at grid side 1, (d) load-shifting profile at grid side 2.

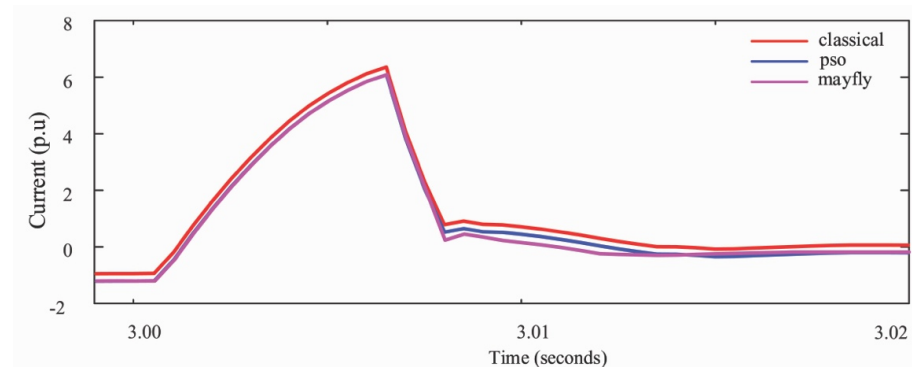


Figure 19. Fault introduction at grid side 2.

9. Conclusions

This scientific paper proposes the use of the Mayfly algorithm, a multi-objective model based on a meta-heuristic optimization technique, to optimally tune the VSC control parameters in the MTDC system. The simultaneous optimization of the VSC control framework, i.e., OCL and ICC control parameters, using the proposed multi-objective MA technique, reduces the computational cost and improves dynamic performance. Meanwhile, the optimized parameters are embedded in a four-terminal, VSC-based MTDC test system in PSCAD/EMTDC to evaluate control performance. A comparison of the proposed scheme with the classical and PSO algorithm is also presented under the same environment. The results verify that the proposed algorithm's ITEA is superior to the classical and PSO models. Under three states: (i) wind-farm power variations, (ii) AC grid-load demand variations, and (iii) permanent VSC disconnection, the simulation test bench is evaluated for classical, PSO, and the proposed multi-objective MA technique. According to the simulation results, the anticipated multi-objective MA algorithm improved the VSC-based control framework under steady-state and dynamic operations compared to other controllers. The stability margin and rise time were greatly improved at both off-shore and on-shore stations.

In future work, the proposed algorithm will be verified using real-world data and implemented on a microprocessor relay with detailed DC line modeling. It will also be compared with recent techniques such as improved teaching–learning-based optimization (ITLBO), Grey Wolf Optimizer (GWO), Model Predictive Control (MPC), and Harris hawks optimization (HHO) models. Moreover, an optimized multi-objective P.I.-controller for multiple VSCs would be developed considering the wind uncertainty.

Author Contributions: Conceptualization, A.R., G.A. and M.Z.Y.; methodology, A.R., G.A., M.Z.Y. and A.R.Y.; software, A.R., M.Z.Y., G.A., A.R.Y. and N.U.; validation, A.R., G.A. and M.Z.Y., A.A.A.-A.; mathematical analysis, A.R., M.Z.Y. and M.J.; investigation, M.J. and M.Z.Y.; resources, A.R., G.A. and M.Z.Y.; writing—original draft preparation, A.R., M.Z.Y. and M.J.; writing—review and editing, A.R., G.A., A.R.Y., M.Z.Y., A.A.A.-A., N.U. and M.J.; visualization, A.R.; supervision, A.R.; project administration, A.R. and M.Z.Y.; funding acquisition, A.A.A.-A. and N.U. All authors have read and agreed to the published version of the manuscript.

Funding: This research work is supported by Taif University Researchers Supporting Project number (TURSP-2020/121), Taif University, Taif, Saudi Arabia.

Institutional Review Board Statement: Not applicable.

Informed Consent Statement: Not applicable.

Data Availability Statement: Not applicable.

Acknowledgments: The authors acknowledge the financial support from Taif University Researchers Supporting Project Number (TURSP-2020/121), Taif University, Saudi Arabia. The authors are grateful to the Guangxi University, Nanning, China, the University of Engineering & Technology, Lahore, Pakistan, and the University of Lahore, Lahore, Pakistan, for providing the facilities to conduct this research.

Conflicts of Interest: The authors declare no conflict of interest.

References

1. Irnawan, R.; da Silva, F.F.; Bak, C.L.; Bregnhøj, T.C. In an initial topology of multi-terminal HVDC transmission system in Europe: A case study of the North-Sea region. In Proceedings of the 2016 IEEE International Energy Conference (ENERGYCON), Leuven, Belgium, 4–8 April 2016; pp. 1–6.
2. Abbas, A.S.; El-Sehiemy, R.A.; El-Ela, A.; Ali, E.S.; Mahmoud, K.; Lehtonen, M.; Darwish, M.M. Optimal Harmonic Mitigation in Distribution Systems with Inverter Based Distributed Generation. *Appl. Sci.* **2021**, *11*, 774. [CrossRef]
3. Icaza, D.; Borge-Diez, D.; Galindo, S.P. Analysis and proposal of energy planning and renewable energy plans in South America: Case study of Ecuador. *Renew. Energy* **2022**, *182*, 314–342. [CrossRef]
4. Liang, X.; Abbasipour, M. HVDC Transmission and Its Potential Application in Remote Communities: Current Practice and Future Trends. *IEEE N. Y.* **2022**, *58*, 1706–1719. [CrossRef]
5. Liang, J.; Jing, T.; Gomis-Bellmunt, O.; Ekanayake, J.; Jenkins, N. Operation and control of multi-terminal HVDC transmission for off-shore wind farms. *IEEE Trans. Power Deliv.* **2011**, *26*, 2596–2604. [CrossRef]
6. Rouzbehi, K.; Candela, J.I.; Luna, A.; Gharehpetian, G.B.; Rodriguez, P. Flexible control of power flow in multi-terminal DC grids using DC–DC converter. *IEEE J. Emerg. Sel. Top. Power Electron.* **2016**, *4*, 1135–1144. [CrossRef]
7. Rouzbehi, K.; Miranian, A.; Candela, J.I.; Luna, A.; Rodriguez, P. A generalized voltage droop strategy for control of multi-terminal DC grids. *IEEE Trans. Ind. Appl.* **2014**, *51*, 607–618. [CrossRef]
8. Rouzbehi, K.; Zhang, W.; Candela, J.I.; Luna, A.; Rodriguez, P. Unified reference controller for flexible primary control and inertia sharing in multi-terminal voltage source converter-HVDC grids. *IET Gener. Transm. Distrib.* **2017**, *11*, 750–758. [CrossRef]
9. Rao, H. Architecture of Nanao multi-terminal VSC-HVDC system and its multi-functional control. *CSEE J. Power Energy Syst.* **2015**, *1*, 9–18. [CrossRef]
10. Li, Y.; Huang, X.; Zhang, J.; Sun, W. China Upgrades Capacity to the Zhoushan Islands: State Grid Corporation Installs First HVDC Five-Terminal Voltage Source Converter Project. Available online: <https://www.tdworld.com/digital-innovations/article/20969421/china-upgrades-capacity-to-the-zhoushan-islands> (accessed on 22 February 2022).
11. Emara, D.; Ezzat, M.; Abdelaziz, A.Y.; Mahmoud, K.; Lehtonen, M.; Darwish, M.M. Novel control strategy for enhancing microgrid operation connected to photovoltaic generation and energy storage systems. *Electronics* **2021**, *10*, 1261. [CrossRef]
12. Ali, M.N.; Soliman, M.; Mahmoud, K.; Guerrero, J.M.; Lehtonen, M.; Darwish, M.M. Resilient Design of Robust Multi-Objectives PID Controllers for Automatic Voltage Regulators: D-Decomposition Approach. *IEEE Access* **2021**, *9*, 106589–106605. [CrossRef]
13. Bendary, A.F.; Abdelaziz, A.Y.; Ismail, M.M.; Mahmoud, K.; Lehtonen, M.; Darwish, M.M. Proposed ANFIS based approach for fault tracking, detection, clearing and rearrangement for photovoltaic system. *Sensors* **2021**, *21*, 2269. [CrossRef] [PubMed]
14. Wu, G.; Liang, J.; Zhou, X.; Li, Y.; Egea-Alvarez, A.; Li, G.; Peng, H.; Zhang, X. Analysis and design of vector control for VSC-HVDC connected to weak grids. *CSEE J. Power Energy Syst.* **2017**, *3*, 115–124. [CrossRef]
15. Sánchez-Sánchez, E.; Prieto-Araujo, E.; Gomis-Bellmunt, O.; Galceran-Arellano, S. Systematic and optimal design of droop-controlled MMCs in MT-HVDC networks. *Int. J. Electr. Power Energy Syst.* **2022**, *138*, 107873. [CrossRef]
16. Raza, A.; Dianguo, X.; Yuchao, L.; Xunwen, S.; Williams, B.; Cecati, C. Coordinated operation and control of VSC based multiterminal high voltage DC transmission systems. *IEEE Trans. Sustain. Energy* **2015**, *7*, 364–373. [CrossRef]
17. Siad, S.B.; Iovine, A.; Damm, G.; Galai-Dol, L.; Netto, M. Nonlinear Hierarchical Easy-to-Implement Control for DC MicroGrids. *Energies* **2022**, *15*, 969. [CrossRef]
18. Mahmoud, H.Y.; Hasanien, H.M.; Besheer, A.H.; Abdelaziz, A.Y. Hybrid cuckoo search algorithm and grey wolf optimiser-based optimal control strategy for performance enhancement of HVDC-based offshore wind farms. *IET Gener. Transm. Distrib.* **2020**, *14*, 1902–1911. [CrossRef]
19. Babes, B.; Rahmani, L.; Chaoui, A.; Hamouda, N. Design and experimental validation of a digital predictive controller for variable-speed wind turbine systems. *J. Power Electron.* **2017**, *17*, 232–241. [CrossRef]
20. Hua, H.; Cao, J.; Yang, G.; Ren, G. Voltage control for uncertain stochastic nonlinear system with application to energy Internet: Non-fragile robust H_∞ approach. *J. Math. Anal. Appl.* **2018**, *463*, 93–110. [CrossRef]
21. Blondin, M.J. *Controller Tuning Optimization Methods for Multi-Constraints and Nonlinear Systems: A Metaheuristic Approach*; Springer: Berlin/Heidelberg, Germany, 2021.
22. Lotfy, M.E.; Senjyu, T.; Farahat, M.A.; Abdel-Gawad, A.F.; Yona, A. Enhancement of a small power system performance using multi-objective optimization. *IEEE Access* **2017**, *5*, 6212–6224. [CrossRef]
23. Lin, L.; Li, A.; Xu, C.; Wang, Y. Multi-objective genetic algorithm based coordinated second-and third-order harmonic voltage injection in modular multilevel converter. *IEEE Access* **2020**, *8*, 94318–94329. [CrossRef]
24. Xu, Y. Building performance optimization for university dormitory through integration of digital gene map into multi-objective genetic algorithm. *Appl. Energy* **2022**, *307*, 118211.
25. Faisal, S.F.; Beig, A.R.; Thomas, S. Time domain particle swarm optimization of PI controllers for bidirectional VSC HVDC light system. *Energies* **2020**, *13*, 866. [CrossRef]
26. Raza, A.; Yousaf, Z.; Jamil, M.; Gilani, S.O.; Abbas, G.; Uzair, M.; Shaheen, S.; Benrabah, A.; Li, F. Multi-objective optimization of VSC stations in multi-terminal VSC-HVdc grids, based on PSO. *IEEE Access* **2018**, *6*, 62995–63004. [CrossRef]

27. Shami, T.M.; El-Saleh, A.A.; Alswaitti, M.; Al-Tashi, Q.; Summakieh, M.A.; Mirjalili, S. Particle Swarm Optimization: A Comprehensive Survey. *IEEE Access* **2022**, *10*, 10031–10061. [[CrossRef](#)]
28. Bibaya, L.; Liu, C.; Li, G. Optimal control tuning of VSC-MTDC using a multi-objective hybrid pso algorithm. In Proceedings of the 2018 2nd IEEE Conference on Energy Internet and Energy System Integration (EI2), Beijing, China, 20–22 October 2018; pp. 1–6.
29. Bhattacharyya, T.; Chatterjee, B.; Singh, P.K.; Yoon, J.H.; Geem, Z.W.; Sarkar, R. Mayfly in harmony: A new hybrid meta-heuristic feature selection algorithm. *IEEE Access* **2020**, *8*, 195929–195945. [[CrossRef](#)]
30. Zervoudakis, K.; Tsafarakis, S. A mayfly optimization algorithm. *Comput. Ind. Eng.* **2020**, *145*, 106–559. [[CrossRef](#)]
31. Li, M.; Chen, H.; Shi, X.; Liu, S.; Zhang, M.; Lu, S. A multi-information fusion “triple variables with iteration” inertia weight PSO algorithm and its application. *Appl. Soft Comp.* **2019**, *84*, 105677. [[CrossRef](#)]
32. Khan, M.A.; Li, X.; Yousaf, M.Z.; Mustafa, A.; Wei, M. Metaheuristic Based Solution for the Non-Linear Controller of the Multiterminal High-Voltage Direct Current Networks. *Energies* **2021**, *14*, 1578. [[CrossRef](#)]
33. Ali, E.S.; El-Sehiemy, R.A.; El-Ela, A.; Adel, A.; Mahmoud, K.; Lehtonen, M.; Darwish, M.M. An effective Bi-stage method for renewable energy sources integration into unbalanced distribution systems considering uncertainty. *Processes* **2021**, *9*, 471. [[CrossRef](#)]
34. Guo, X.; Yan, X.; Jermisittiparsert, K. Using the modified mayfly algorithm for optimizing the component size and operation strategy of a high temperature PEMFC-powered CCHP. *Energy Rep.* **2021**, *7*, 1234–1245. [[CrossRef](#)]
35. Majumdar, K.; Roy, P.K.; Banerjee, S. Multi-objective chaotic mayfly optimization for solar-wind-hydrothermal scheduling based on atc problem. *Int. J. Power Energy Syst.* **2022**, *42*, 1–8. [[CrossRef](#)]
36. Yousaf, M.Z.; Shahid, M.A.; Khan, D.; Khalid, S. Improved Coordinated Control of AVM based Multi-Terminal HVdc System using Steady-State Analysis. *Int. J. Electr. Eng. Inform.* **2020**, *12*, 296–321.
37. Marler, R.T.; Arora, J.S. The weighted sum method for multi-objective optimization: New insights. *Struct. Multidiscip. Optim.* **2010**, *41*, 853–862. [[CrossRef](#)]
38. Rodrigues, S.; Pinto, R.T.; Bauer, P. *Dynamic Modeling and Control of VSC-Based Multi-Terminal DC Networks: With Focus on off-Shore Wind Energy Systems*; Lap Lambert Academic Publishing: Chişinău, Moldova, 2012.
39. Helmi, A.M.; Carli, R.; Dotoli, M.; Ramadan, H.S. Efficient and sustainable reconfiguration of distribution networks via metaheuristic optimization. *IEEE Trans. Autom. Sci. Eng.* **2021**, *19*, 82–98. [[CrossRef](#)]
40. Muhammad, M.A.; Mokhlis, H.; Naidu, K.; Amin, A.; Franco, J.F.; Othman, M. Distribution network planning enhancement via network reconfiguration and DG integration using dataset approach and water cycle algorithm. *J. Mod. Power Syst. Clean Energy* **2019**, *8*, 86–93. [[CrossRef](#)]
41. Amin, M.; Molinas, M. Model Predictive Control of Voltage Source Converter in a HVDC System. *arXiv* **2017**, arXiv:1704-04293.